

Lawrence Berkeley National Laboratory

LBL Publications

Title

The structural basis for the functional comparability of factor VIII and the long-acting variant recombinant factor VIII Fc fusion protein

Permalink

<https://escholarship.org/uc/item/82c7d83v>

Journal

Journal of Thrombosis and Haemostasis, 15(6)

ISSN

1538-7933

Authors

Leksa, NC

Chiu, P-L

Bou-Assaf, GM

et al.

Publication Date

2017-06-01

DOI

10.1111/jth.13700

Peer reviewed

ORIGINAL ARTICLE

The structural basis for the functional comparability of factor VIII and the long-acting variant recombinant factor VIII Fc fusion protein

N. C. LEKSA,*¹ P.-L. CHIU,†² G. M. BOU-ASSAF,* C. QUAN,* Z. LIU,*³ A. B. GOODMAN,*¹ M. G. CHAMBERS,† S. E. TSUTAKAWA,‡ M. HAMMEL,‡ R. T. PETERS,*¹ T. WALZ*§ and J. D. KULMAN*⁴

*Biogen, Cambridge; †Department of Cell Biology, Harvard Medical School, Boston, MA; ‡Molecular Biophysics & Integrated Bioimaging, Lawrence Berkeley National Laboratory, Berkeley, CA; and §Laboratory of Molecular Electron Microscopy, Rockefeller University, New York, NY, USA

To cite this article: Leksa NC, Chiu P-L, Bou-Assaf GM, Quan C, Liu Z, Goodman AB, Chambers MG, Tsutakawa SE, Hammel M, Peters RT, Walz T, Kulman JD. The structural basis for the functional comparability of factor VIII and the long-acting variant recombinant factor VIII Fc fusion protein. *J Thromb Haemost* 2017; **15**: 1167–79.

Essentials

- Recombinant factor VIII (rFVIII) Fc fusion protein has a 1.5-fold longer half-life than rFVIII.
- Five orthogonal methods were used to characterize the structure of rFVIII-Fc compared to rFVIII.
- The C-terminal Fc fusion does not perturb the structure of FVIII in rFVIII-Fc.
- The FVIII and Fc components of rFVIII-Fc are flexibly tethered and functionally independent.

Summary. *Background:* Fusion of the human IgG₁ Fc domain to the C-terminal C2 domain of B-domain-deleted (BDD) factor VIII (FVIII) results in the recombinant FVIII Fc (rFVIII-Fc) fusion protein, which has a 1.5-fold longer half-life in humans. *Objective:* To assess the structural properties of rFVIII-Fc by comparing its constituent FVIII and Fc elements with their respective isolated components, and evaluating their structural independence within rFVIII-Fc. *Methods:* rFVIII-Fc and its

isolated FVIII and Fc components were compared by the use of hydrogen–deuterium exchange mass spectrometry (HDX-MS). The structure of rFVIII-Fc was also evaluated by the use of X-ray crystallography, small-angle X-ray scattering (SAXS), and electron microscopy (EM). The degree of steric interference by the appended Fc domain was assessed by EM and surface plasmon resonance (SPR). *Results:* HDX-MS analysis of rFVIII-Fc revealed that fusion caused no structural perturbations in FVIII or Fc. The rFVIII-Fc crystal structure showed that the FVIII component is indistinguishable from published BDD FVIII structures. The Fc domain was not observed, indicating high mobility. SAXS analysis was consistent with an ensemble of rigid-body models in which the Fc domain exists in a largely extended orientation relative to FVIII. Binding of Fab fragments of anti-C2 domain antibodies to BDD FVIII was visualized by EM, and the affinities of the corresponding intact antibodies for BDD FVIII and rFVIII-Fc were comparable by SPR analysis. *Conclusions:* The FVIII and Fc components of rFVIII-Fc are structurally indistinguishable from their isolated constituents, and show a high degree of structural independence, consistent with the functional comparability of rFVIII-Fc and unmodified FVIII.

Correspondence: Nina Leksa, Bioverativ Therapeutics, 225 Second Avenue, Waltham MA, 02142, USA.
Tel.: +1 781 663 1861; fax: +1 781 663 4991.
E-mail: nina.leksa@bioverativ.com

¹Present address: Bioverativ Therapeutics, Waltham, MA, USA

²Present address: School of Molecular Sciences, Biodesign Institute, Arizona State University, Tempe, AZ, USA

³Present address: Compass Therapeutics, Cambridge, MA, USA

⁴Present address: Codiak BioSciences, Cambridge, MA, USA

Received 9 February 2017

Manuscript handled by: D. DiMichele

Final decision: P. H. Reitsma, 28 March 2017

Keywords: B-domain-deleted factor VIII; bleeding; factor VIII; hemophilia A; rFVIII-Fc protein.

Introduction

Hemophilia A is an X-linked bleeding disorder caused by a functional deficiency of coagulation factor VIII (FVIII) [1]. Individuals with hemophilia A are treated with intravenous infusions of FVIII. For severe hemophilia A, routine prophylaxis entails frequent injections, typically three

times weekly or every other day, depending on an individual's pharmacokinetic (PK) profile [2,3]. To increase FVIII activity levels, efforts were initiated to develop long-acting FVIII variants, which would also allow for less frequent injections [4]. Strategies for extending the circulating half-life of FVIII include the generation of a variety of FVIII–polyethylene glycol (PEG) adducts [5–9] and fusion of an IgG₁ Fc domain [10]. The recombinant FVIII Fc (rFVIII-Fc) fusion protein, in which the Fc domain is fused to the C terminus of B-domain-deleted (BDD) FVIII, has been extensively characterized. Importantly, the specific activity of rFVIII-Fc and its affinity for von Willebrand factor (VWF) were comparable to those of other recombinant FVIII products [11]. Preclinical animal studies have shown that rFVIII-Fc is well tolerated in both monkeys and rats [12], and clinical data from the ALONG and ASPIRE trials confirm the long-term safety of rFVIII-Fc and the maintenance of a low annualized bleeding rate with extended-interval prophylactic dosing in patients with severe hemophilia A [13–15].

Although the *in vivo* efficacy, biochemical properties and PK profile of rFVIII-Fc have been extensively investigated, the structural implications of fusing an Fc to the FVIII C2 domain have not been previously reported. The importance of the C2 domain in mediating interactions between FVIII and both phospholipids and VWF is well documented [16–18]. Electron microscopy (EM) studies have provided a first glimpse of the FVIII–VWF complex structure, and corroborated previous findings that the C1 domain of FVIII is the primary interaction site for VWF, with the C2 domain playing an ancillary role [19,20]. Additionally, the C2 domain has been shown to be immunodominant, with many neutralizing antibodies targeting this domain having been identified in inhibitor patient plasmas [21,22]. These antibodies interfere with the ability of FVIII to bind VWF and phospholipids, or slow the release of thrombin-activated FVIII from VWF, thereby inhibiting its activity. In contrast, rFVIII-Fc retains normal VWF and phospholipid binding, and also retains the molar specific activity of unmodified FVIII. To reconcile these observations, we assessed the structure of the individual FVIII and Fc components of rFVIII-Fc and the spatial relationship between them with a variety of orthogonal methods. Our studies show that the appended Fc does not alter the structure of the FVIII portion of rFVIII-Fc, and that these two elements are flexibly tethered, allowing for translational and rotational freedom about the FVIII–Fc fusion site.

Materials and methods

Protein expression and purification

rFVIII-Fc was expressed in HEK293 cells and purified as described previously [11,23,24]. Recombinant human BDD factor VIII (rFVIII) was expressed and purified as

described previously [23], loaded onto a trimethylaminoethyl column (Fractogel EMD TMAE HiCap [M]; EMD Millipore, Billerica, MA, USA), and eluted with a linear NaCl gradient (75 mM to 0.75 M). Recombinant human IgG₁ Fc domain (rFc) was expressed by transient transfection of HEK293 cells, and purified by affinity chromatography on a MabSelect SuRe column (GE Healthcare, Piscataway, NJ, USA) and size-exclusion chromatography on a Superdex 200 column.

ESH8 mAb (Sekisui Diagnostics, Stamford, CT, USA) was cleaved with papain (Roche, Indianapolis, IN, USA), and purified by size-exclusion chromatography on a Superdex 200 column. GMA-8014 Fab and GMA-8008 Fab were purchased from Green Mountain Antibodies (Burlington, VT, USA).

Hydrogen–deuterium exchange mass spectrometry (HDX-MS)

rFVIII-Fc, rFVIII and rFc were dialyzed against 10 mM histidine (pH 7.0), 5 mM CaCl₂, 200 mM NaCl, and 13.3 g L⁻¹ sucrose. Deuterium exchange was initiated by diluting each sample 10-fold with deuterated buffer (99.99% D₂O; Cambridge Isotope Laboratories, Andover, MA, USA) to a final volume of 25 µL. After 10 s, 1 min, 10 min, 1 h and 4 h of incubation, the reaction was quenched, and the protein was denatured and reduced by addition of ice-cold quench solution (1 : 1, v/v) containing 7.5 M guanidinium hydrochloride, 0.2 M Tris(2-carboxyethyl)phosphine, and 0.5 M citric acid, resulting in a pH of 2.3. This preparation was digested on an immobilized pepsin column (Life Technologies, Carlsbad, CA, USA) inside a Waters HDX manager with the temperature maintained at 0 °C. Eluted peptides were desalted, separated on an HSS T3 C18 HPLC column, and introduced into a Synapt G2S mass spectrometer by electrospray ionization. Mass spectra were collected in triplicate for each exchange period. Peptides were identified by use of PROTEINLYNX GLOBAL SERVER (Waters, Milford, MA, USA).

HDX data analysis was performed with the DYNAMX software package (Waters), and statistical relevance was based on published criteria [25].

X-ray crystallography

Crystallization and data collection rFVIII-Fc was dialyzed into 25 mM HEPES (pH 7.5), 550 mM NaCl, and 5 mM CaCl₂, and concentrated to 8 mg mL⁻¹. Crystallization was performed with the nanodroplet vapor diffusion method at 4 °C by mixing 200 nL of protein solution with 200 nL of the reservoir solution containing 5% ethanol and 100 mM Tris (pH 7.3). Crystals were cryoprotected by gradual addition of propanediol to the reservoir liquor to 25% (v/v) without ethanol, and flash-frozen in liquid nitrogen. Diffraction data were collected

at the Advanced Photon Source (APS) at Lilly Research Laboratories Collaborative Access Team (LRL-CAT) at $-173\text{ }^{\circ}\text{C}$ with the MAR225 CCD detector.

Structure determination and refinement Data reduction was carried out with HKL2000 [26]. The space group was $P4_12_1$. The rFVIII_{FC} structure was solved by molecular replacement with the program PHASER [27] and the FVIII crystal structure (Protein Data Bank [PDB] code 2R7E [28]) as the search model. COOT [29] was used for model building, and REFMAC5 was used for refinement with external restraints from the initial search model as a reference structure by the use of PROSMART [30–32]. For later stages of refinement, TLS refinement [33] with anisotropic motion tensors was used. Figures were prepared with PYMOL [34]. Data collection and refinement statistics are summarized in Table S1.

Small-angle X-ray scattering (SAXS) data collection and evaluation

SAXS data of freshly gel-filtered samples were collected at ALS beamline 12.3.1 (Lawrence Berkeley National Laboratory, Berkeley, CA, USA) [35,36]. The wavelength was set to $1.03\text{ }\text{\AA}$, and the sample-to-detector distance to 1.5 m , resulting in scattering vectors, q , ranging from $0.01\text{ }\text{\AA}^{-1}$ to $0.32\text{ }\text{\AA}^{-1}$. Experiments were performed at $15\text{ }^{\circ}\text{C}$, and data were processed as described previously [36]. Briefly, the data acquired at five exposures (0.5, 0.5, 2, 5 and 0.5 s) were merged for calculations using the entire scattering profile. The experimental SAXS curves for different time exposures were investigated for aggregation by the use of Guinier plots [37]. The radius of gyration, R_G , was derived by the Guinier approximation $I(q) = I(0) \exp(-q^2 R_G^2/3)$ with the limit $q R_G < 1.6$ (Fig. S1). The program SCATTER was used to compute the experimental and models pair distance distribution functions, $P(r)$ (Fig. S1B,C), providing the maximum dimension of the macromolecule, D_{\max} . Data collection details and SAXS parameters are listed in Table S2. Theoretical scattering profiles were calculated with FOXS [38]. With a rigid-body modeling strategy, BILBOMD, simulations were used to explore the conformational space adopted by the C-terminally fused Fc domain. A minimal ensemble search (MES) was used to identify the minimal ensemble required to best fit the experimental data [39].

EM

Image acquisition An rFVIII_{FC} sample was adsorbed to glow-discharged, carbon-coated grids, and negatively stained as described previously [40]. Low-dose images were collected with a $4\text{K} \times 4\text{K}$ CCD camera (Gatan, Pleasanton, CA, USA) on a Tecnai T12 electron microscope (FEI, Hillsboro, OR, USA) operated at an acceleration voltage of 120 kV . The calibrated magnification

was $\times 70\,527$ (nominal magnification of $\times 52\,000$), yielding a pixel size of $2.13\text{ }\text{\AA}$ at the specimen level. The defocus was set to $-1.5\text{ }\mu\text{m}$. Specimen areas used for three-dimensional (3D) reconstructions were imaged twice, first at a tilt angle of 60° and then again untilted (Fig. S2).

Image processing The SPIDER software [41] was used to select 16 158 particle pairs from 112 image pairs, which were windowed into 128×128 -pixel images. For the iterative stable alignment and clustering (ISAC) algorithm [42] implemented in SPARX [43], the particle images from the untilted specimen were reduced to 64×64 pixels. With specification of 50 images per group and a pixel error threshold of 0.7, 25 generations of ISAC yielded 475 classes (Fig. S3), accounting for 9284 particles (57.5% of the entire dataset). To visualize the mobility of the Fc domain, selected ISAC averages were aligned to each other, ordered according to their correlation coefficients, and used to prepare Movie S1.

For 3D reconstruction, the particle images from the untilted specimen were subjected to 10 cycles of reference-free alignment and conventional K -means classification into 100 classes in SPIDER. From the resulting class averages (Fig. S4A), seven averages were used as references for one cycle of supervised classification (Fig. S4B). The particles from the tilted specimen of the resulting groups were used to calculate random conical tilt 3D reconstructions [44] that were refined with projection matching [45], resulting in six interpretable density maps with resolutions from 2.5 nm to 3 nm according to the Fourier shell correlation = 0.5 criterion [46] (Fig. S5). The UCSF CHIMERA software [47] was used to visualize the 3D maps and to place the crystal structures of FVIII (PDB code 3CDZ) and Fc (PDB code 1HZH) into the maps (Fig. S6).

For rFVIII–Fab complexes, BOXER of the EMAN software package [48] was used to select 5013 particles from 45 images for 1B5 (GMA-8008), 5250 particles from 20 images for 3G6 (GMA-8014), and 5103 particles from 50 images for ESH8. The particles were windowed into 120×120 -pixel images, and subjected to 10 cycles of reference-free alignment and K -means classification into 25 classes in SPIDER.

Surface plasmon resonance (SPR) analysis

The affinities of rFVIII and rFVIII_{FC} for mAbs 1B5 (GMA-8008), 3G6 (GMA-8014) and ESH8 were determined by ‘one-shot’ kinetics with a ProteOn XPR36 interaction array system (BioRad, Hercules, CA, USA) [49]. Briefly, goat α -mouse antibody (Jackson ImmunoResearch, West Grove, PA, USA) at a concentration of $30\text{ }\mu\text{g mL}^{-1}$ in 10 mM sodium acetate (pH 5) was immobilized in channels of a GLC sensor chip (BioRad) by EDC/Sulfo-NHS amine coupling followed by blocking with ethanolamine. All three anti-FVIII antibodies were subsequently captured to a level of ~ 70 resonance units.

Each of the BDD rFVIII and rFVIII-Fc analytes was applied in a direction perpendicular to that used for the capture of the antibodies at concentrations of 0.07, 0.2, 0.6, 1.8 and 5.4 nM in phosphate-buffered saline (pH 7.4) containing 0.005% Tween-20 (PBST) for 6 min, and this was followed by a dissociation phase (in PBST alone) of 29 min. Binding experiments were performed in triplicate at a flow rate of 30 $\mu\text{L min}^{-1}$ at 25 °C on the same sensor chip. Raw data were processed by buffer blank subtraction and interspot referencing, and kinetic parameters were derived with the PROTEON MANAGER software by applying a 1 : 1 interaction model that yielded values for χ^2/R_{max} of 0.05 or less.

Results

HDX-MS of rFVIII-Fc, rFVIII, and Fc

HDX-MS was performed with rFVIII-Fc, rFVIII and Fc to determine whether the fusion of Fc to FVIII results in the structural perturbation of either component. Peptide coverage ranged from 87% to 97% (Fig. S7), and the deuterium exchange of the FVIII and Fc portions of rFVIII-Fc was compared with that of the isolated constituents (Fig. 1). On the basis of established criteria [25], no regions of differential deuterium exchange were found to be statistically significant, indicating that the structure of FVIII is unaffected by C-terminal Fc fusion. Notably, the lack of differential deuterium exchange proximal to the fusion site implies that Fc neither directly abuts FVIII nor distorts its tertiary structure.

X-ray crystallography of rFVIII-Fc

We crystallized rFVIII-Fc, which consists of a heavy chain (domains A1 and A2) and a light chain (domains A3, C1, and C2) of FVIII, and a monomeric Fc fused to the C terminus of the C2 domain. The C-terminal Fc fusion forms a dimer with a separately expressed monomeric Fc domain to form the full assembly. At 4.2-Å resolution, the overall structure of BDD FVIII in rFVIII-Fc, and that of each of its five individual domains, were similar to the previously solved structures of BDD FVIII alone (PDB code 2R7E, 3.7-Å resolution [26]; PDB code 3CDZ, 3.98-Å resolution [41]), and superimposed with a root mean square deviation of 0.83–1.58 Å (Fig. 2A; Table 1). The most significant differences between structures were found in loop regions, and several loops have, in fact, been omitted from both published structures and from our rFVIII-Fc structure, owing to poor electron density. Furthermore, the locations of bound metal ions and glycosylation sites were also conserved, as previously shown [11]. Whereas the heavy chain, light chain–Fc fusion and monomeric Fc were all present in the crystal (Fig. S8), no electron density was observed for Fc, indicating that it was disordered in the crystal lattice. Analysis of the

crystal packing revealed a large solvent channel (approximately 60 × 70 × 75 Å) located at the C terminus of the C2 domain, where Fc is expected to be (Fig. 2B). The channel was sufficient in volume to accommodate the various Fc conformations observed with SAXS and EM (see below). In Fig. 2B, we have modeled one such conformation by using one of the positions of Fc seen in the EM maps, illustrating that Fc can easily fit into the solvent channel. Taken together, these data suggest that Fc does not alter the atomic structure of FVIII, but rather is flexibly tethered to FVIII.

SAXS of rFVIII and rFVIII-Fc

To assess the structural dynamics of rFVIII-Fc in solution, we collected and analyzed SAXS curves of rFVIII and rFVIII-Fc (Fig. 3A,B). The SAXS profile and linear Guinier plot [37] of rFVIII alone indicated that the protein does not aggregate in solution (Fig. S1A). The pair distribution function $P(r)$ (Fig. 1B) and experimental SAXS curve of rFVIII matched the theoretical $P(r)$ and SAXS profile calculated from an rFVIII model generated by modeling missing loops into the structure of FVIII [28]. Therefore, we also included the missing loops in our solution structure modeling of rFVIII-Fc. To examine the flexible character of the appended Fc domain in rFVIII-Fc, we used rigid-body modeling by BILBOMD [39]. An initial rFVIII-Fc model was built by fusing the structure of the human IgG₁ Fc domain [50] to the rFVIII model described above. A large set of models that represent possible structures of rFVIII-Fc were then generated by allowing the FVIII and Fc portions of rFVIII-Fc to move as rigid bodies relative to one another. From these models, theoretical SAXS curves were calculated and compared with the experimental curve collected for rFVIII-Fc by the use of previously published methods [38]. From all modeled conformers, the best-fitting structure ($\chi = 1.6$) (Fig. 3B) positioned Fc in an extended conformation away from FVIII, consistent with the maximal dimension observed in the $P(r)$ (Fig. S1C). Reconstruction of a single best model for flexible proteins can be misleading and, at best, provides an average of the conformations [51]. Taking into account the likely coexistence of different conformations of the rFVIII-Fc fusion protein, we applied the MES approach to identify the minimal ensemble required to best fit the experimental data [39]. The resulting ensemble model, consisting of three conformers (Fig. 3C), improved the match of the $P(r)$ functions (Fig. S1C) and SAXS profiles ($\chi = 1.4$), particularly in the low-resolution q range ($q < 0.1 \text{ \AA}^{-1}$) (Fig. 3B). These results indicate a high degree of conformational variability about the FVIII–Fc fusion site.

EM of rFVIII-Fc

We used negative-stain EM to visualize rFVIII-Fc. The relative positions of the FVIII domains were the same in

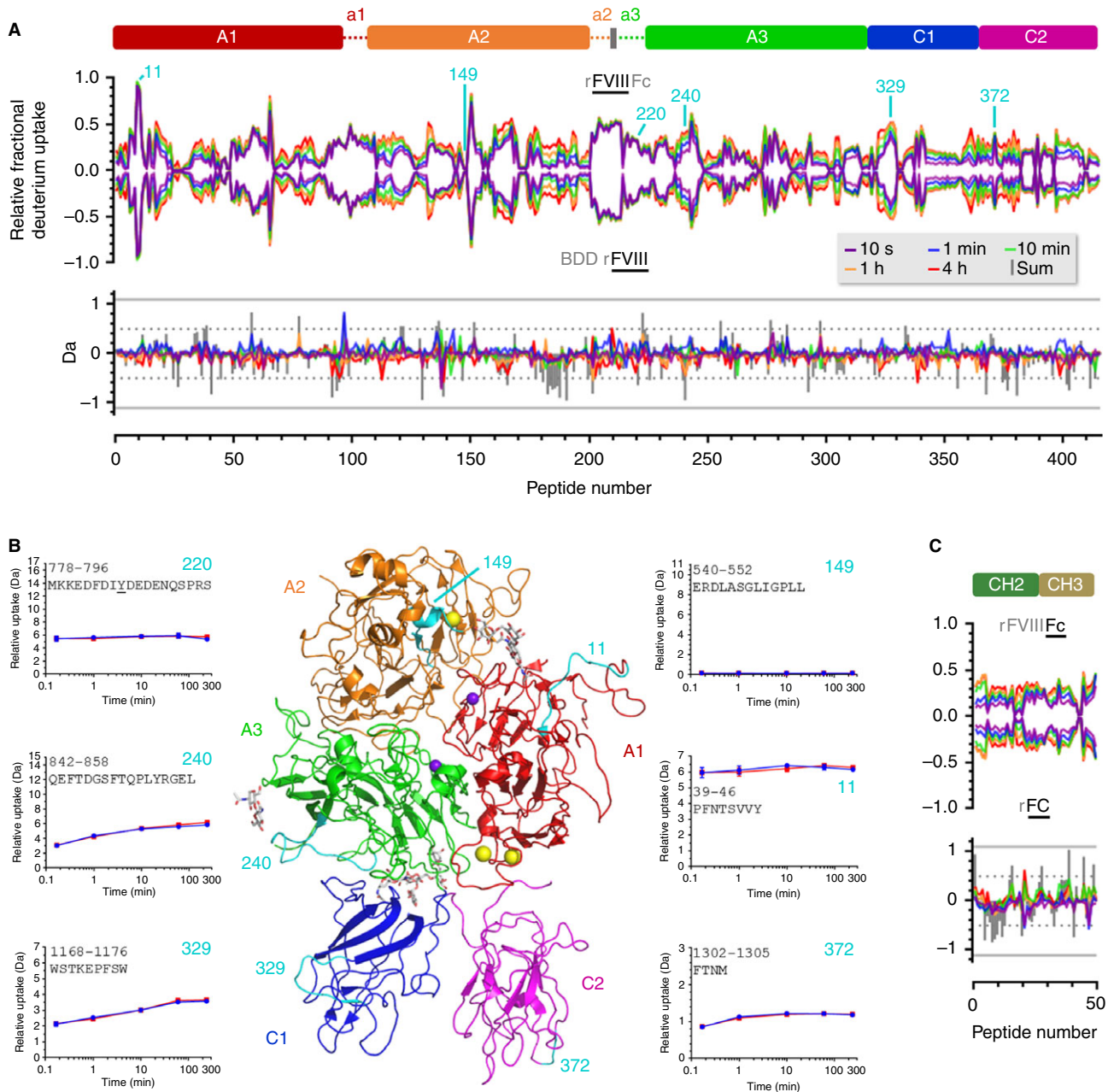


Fig. 1. Structural comparison of recombinant factor VIII Fc (rFVIII_{Fc}) and B-domain-deleted (BDD) recombinant FVIII (rFVIII) by hydrogen–deuterium exchange mass spectrometry. (A) Butterfly plot (top) and difference plot (bottom) comparing deuterium uptake of the FVIII component of rFVIII_{Fc} with that of isolated BDD rFVIII. For the butterfly plot, the y-axis indicates deuterium uptake, expressed as the fraction of exchangeable amide protons displaced by deuterons, for a given peptide derived from rFVIII_{Fc} (positive values) or from BDD rFVIII (negative values). For the difference plot, the y-axis indicates the average ($N = 3$) calculated mass difference (in Da) for peptides derived from rFVIII_{Fc} and BDD rFVIII. The x-axis indicates the 416 FVIII-derived peptides ordered from the N terminus to the C terminus based on their respective midpoints. The corresponding locations of FVIII domains (A1, A2, A3, C1, and C2) are indicated above with solid bars, and those of the acidic a1, a2 and a3 domains are indicated with dashed lines. (B) Selected deuterium uptake plots for FVIII-derived peptides. Peptide numbering (cyan) corresponds to the sequence positions indicated in (A). The domains in the ribbon representation of FVIII (Protein Data Bank code 2R7E) are colored as in (A), and calcium (yellow) and copper (purple) ions are depicted as spheres. (C) Corresponding butterfly plot (top) and difference plot (bottom) for peptides derived from the Fc domain of rFVIII_{Fc} and isolated recombinant Fc. The x-axis indicates the 50 Fc-derived peptides ordered as in (A). The corresponding locations of the CH2 and CH3 subdomains of the Fc domain are indicated with solid bars.

all class averages (Fig. 4A; Fig. S3), but the angle between Fc and FVIII varied greatly. Most averages showed Fc located close to the C2 and A1 domains of

FVIII, but a few showed that Fc can also move to a position below the C1 and C2 domains. Furthermore, Fc can be seen in ‘front’ and ‘side’ views, indicating that there is

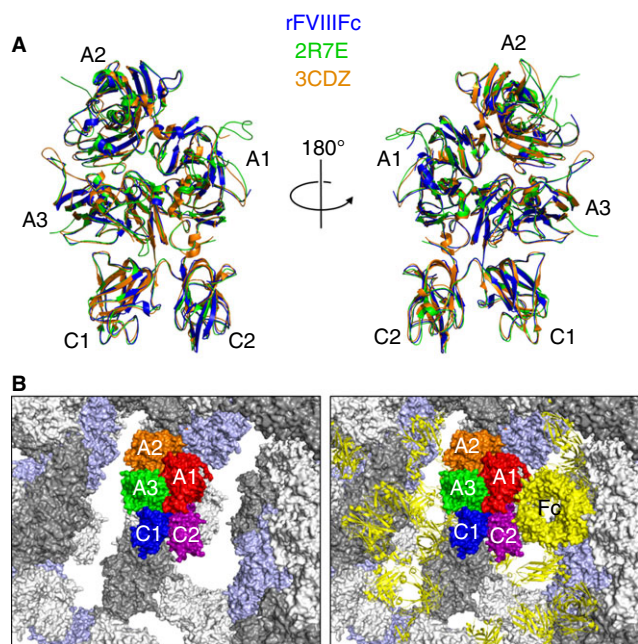


Fig. 2. Crystal structure of recombinant factor VIII Fc (rFVIII Fc). (A) Superposition of the FVIII component of rFVIII Fc (blue) with two previously solved structures of B-domain-deleted FVIII (Protein Data Bank [PDB] code 2R7E, green; PDB code 3CDZ, orange) is shown in two views rotated by 180°. No electron density was observed for Fc, suggesting that it is not ordered in the crystal lattice. (B) The FVIII element of rFVIII Fc is shown in surface representation, with its constituent domains shown in different colors (A1, red; A2, orange; A3, green; C1, blue; C2, purple). Symmetry mates of FVIII are also shown in surface representation, and colored white, gray, and light blue, and reveal the presence of large solvent channels (left panel). One Fc conformation is modeled according to the position of Fc from one of the EM structures (right panel). The Fc is shown in surface representation, and symmetry mates are shown in cartoon representation.

Table 1 C α root mean square deviation (RMSD) values of FVIII structures (Å)

	A1	A2	A3	C1	C2	All
rFVIII Fc: 2R7E	0.84	0.83	0.84	0.90	0.87	1.02
rFVIII Fc: 3CDZ	1.43	1.35	1.26	1.08	0.92	1.58
2R7E: 3CDZ	1.59	1.91	1.51	1.20	1.09	1.59

rFVIII Fc, recombinant human B-domain-deleted FVIII Fc.

also rotational freedom of Fc relative to FVIII. Movie S1 illustrates the substantial mobility of Fc relative to FVIII. Next, 3D maps of rFVIII Fc were created by using the random conical tilt reconstruction method, and these showed flexibility of Fc similar to that seen in the two-dimensional averages (Fig. 4B). Placement of the crystal structures of FVIII [28] and Fc [50] into the 3D maps yielded models of the intact rFVIII Fc molecule (Fig. 4C). These data confirm that Fc is flexibly tethered to FVIII.

EM and SPR analysis of Fab and antibody binding to FVIII

Antibodies against the FVIII C2 domain have been extensively characterized, owing to the prevalence of neutralizing alloantibodies directed against the C2 domain in individuals with hemophilia A who develop inhibitors as a consequence of FVIII replacement therapy [21]. Anti-C2 antibodies have also been used to study the role of the C2 domain in the association of FVIII with phospholipid surfaces and VWF, and in the proteolytic activation of FVIII by thrombin and activated FX (FXa). These antibodies have been categorized into five groups (A, AB, B, BC, and C) on the basis of their respective epitopes, and characterized with regard to their ability to inhibit FVIII activity, phospholipid binding, and VWF binding [21]. More recently, the epitopes of several of these antibodies were fine-mapped by scanning mutagenesis and affinity analysis by SPR [52]. Of these, we selected three antibodies with a range of inhibitory activities and epitopes with varying proximities to the Fc domain fusion site at the C terminus of rFVIII Fc: 1B5 (group B, alias GMA-8008), 3G6 (group BC, alias GMA-8014), and ESH8 (group C) (Fig. 5A). The structures of BDD FVIII in complex with Fab fragments from each of these antibodies were determined by negative-stain EM. Representative class averages (Fig. 5B; see Fig. S9 for all averages) are consistent with previously reported epitopes [52], and indicate varying degrees of conformational flexibility about the FVIII–Fab axis for 1B5 (moderate), 3G6 (low), and ESH8 (moderate). Despite this positional variability, the locations of Fab fragments coincide spatially with areas occupied by the Fc domain of rFVIII Fc as determined here by SAXS (Fig. 3C) and EM (Fig. 4; Movie S1).

The relative affinities of each of these antibodies for BDD rFVIII and rFVIII Fc were determined by SPR. Representative sensorgrams (Fig. 5C) illustrate qualitatively similar dissociation and association kinetics for BDD rFVIII and rFVIII Fc for each antibody, consistent with similar K_D values for each pair of interactions (Table 2). We therefore conclude that BDD rFVIII and rFVIII Fc are similarly able to accommodate the binding of these three anti-C2 antibodies, confirming that the linkage between FVIII and Fc in rFVIII Fc is highly flexible, and that the tethered Fc is relatively unconstrained.

Discussion

Long-acting FVIII molecules allow the achievement of higher factor activity levels and/or less frequent intravenous administration, and represent one of the most significant improvements in the prevailing standard of care for patients with hemophilia A in > 20 years. In addition to Fc fusion, current strategies for extending the half-life of FVIII include chemical conjugation of PEG adducts to FVIII by a variety of methods [53]. Regardless of the

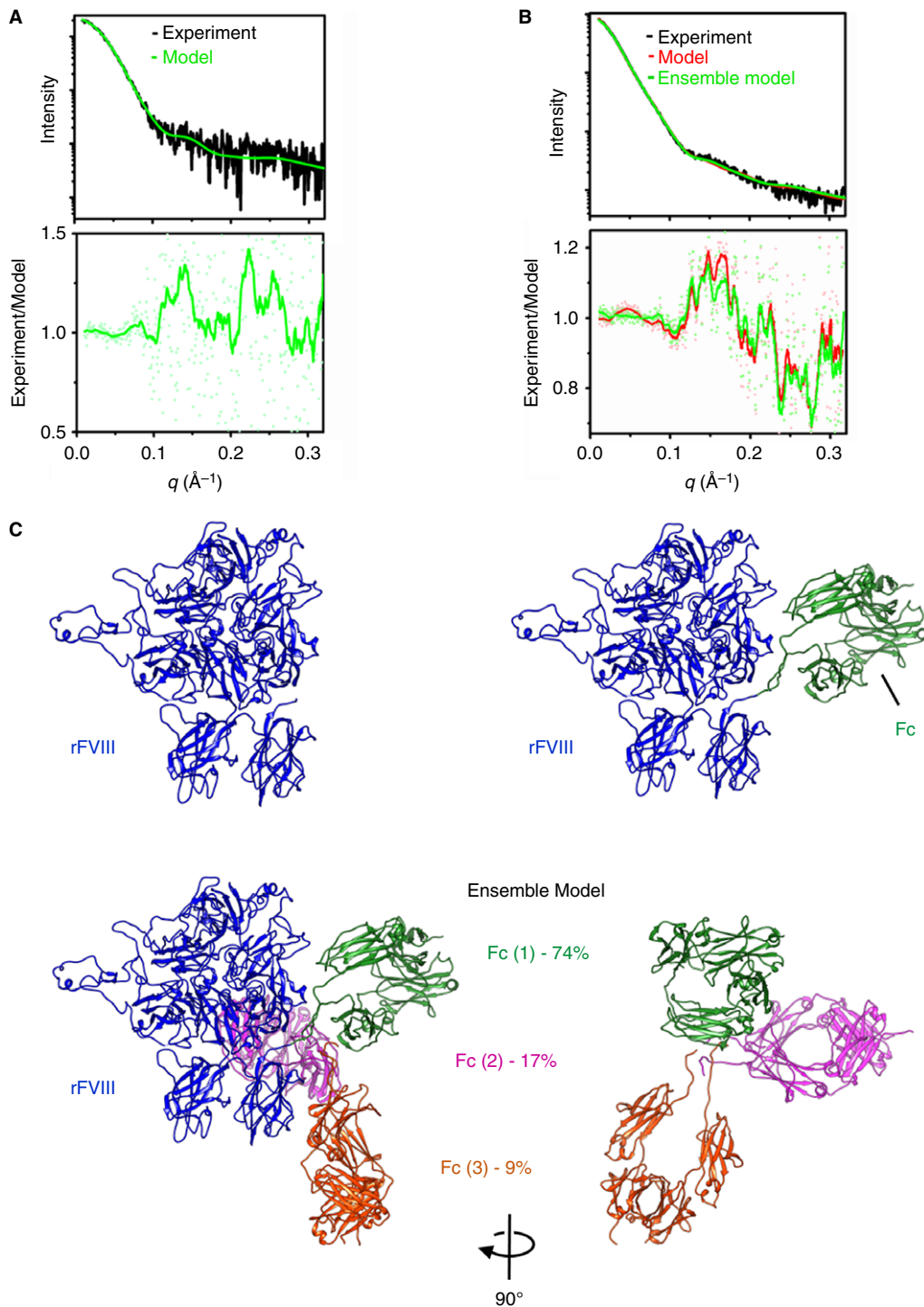


Fig. 3. Solution structure of recombinant factor VIII Fc (rFVIII-Fc). (A) Comparison of the experimental (black) and calculated scattering profiles for the recombinant FVIII (rFVIII) atomistic model (green, $\chi = 1.1$). (B) Comparison of the experimental (black) and calculated scattering profiles for the single best fit model (red, $\chi = 1.6$) and the ensemble model (green, $\chi = 1.4$) of rFVIII-Fc. Residuals are shown below as green and red lines. (C) The atomistic models of rFVIII and rFVIII-Fc (best fit) are shown on top, with FVIII colored in blue and Fc in green. The ensemble model of rFVIII-Fc is shown below, with FVIII colored in blue. The individual Fc conformers are shown in green, pink, and orange, and their weights are indicated. The variable positions of Fc in the ensemble model are also shown rotated by 90° around the y -axis.

approach used to extend the half-life of FVIII, a detailed analysis of the 3D structure of the resulting molecule is essential to ensure the absence of structural perturbations

that could alter its specific activity or bioavailability relative to the original FVIII molecule, or promote the formation of neo-epitopes that could have immunogenic

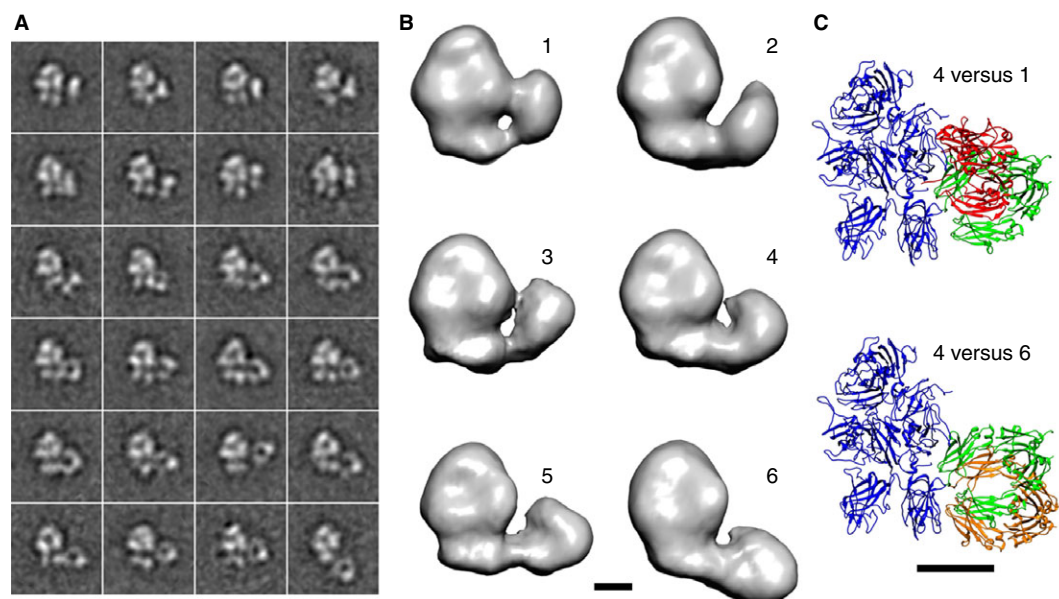


Fig. 4. Single-particle electron microscopy (EM) analysis of negatively stained recombinant factor VIII Fc. (A) Representative class averages obtained with the iterative stable alignment and classification procedure (see Fig. S3 for all averages). The side length of the individual panels is 27.3 nm. (B) 3D maps of six classes. (C) Superposition of models obtained by placing atomic models of FVIII and Fc into EM density maps 1 and 4 (top) and 6 and 4 (bottom). The atomic model of FVIII (Protein Data Bank [PDB] code 3CDZ) is shown in blue, and the atomic models of Fc (PDB code 1HZH) placed into volumes 4, 1 and 6 are shown in green, red, and orange, respectively. Scale bars in (B) and (C): 5 nm.

consequences. For rFVIII-Fc, these concerns have been allayed, in part, by several key findings. First, the specific activity of rFVIII-Fc and its affinity for VWF are indistinguishable from those of BDD rFVIII [11]. Second, in hemophilia A mice, rFVIII-Fc shows reduced immunogenicity relative to BDD rFVIII and full-length rFVIII, and even induces a tolerogenic response [54]. Finally, no incidences of inhibitor formation were observed in the rFVIII-Fc pivotal phase 3 (A-LONG) trial in previously treated patients [13] or in a subsequent clinical trial of 71 previously treated pediatric patients (Kids A-LONG) [55]. These observations suggest structural comparability between the FVIII component of rFVIII-Fc and otherwise unmodified FVIII, consistent with our finding that the structure of the FVIII component of rFVIII-Fc is indistinguishable from two previously published FVIII structures [28,56]. This conclusion is further strengthened by our HDX-MS analysis, which revealed no statistically significant differences in deuterium uptake within 416 individual peptides representing 94% sequence coverage of the FVIII component of rFVIII-Fc or within 50 peptides representing 87% sequence coverage of its Fc domain (Fig. S7).

Our HDX-MS and X-ray crystallographic data also provide insights into the nature of the Fc linkage to FVIII in rFVIII-Fc. The lack of differential deuterium uptake between FVIII with and without the appended Fc domain suggests that any interactions that might occur in solution between Fc and FVIII are sufficiently transient in nature so as to not perturb deuterium uptake in either component when tethered. The lack of visible electron density for Fc in the rFVIII-Fc crystal also implies that Fc adopts various orientations relative to FVIII. These results are consistent with the known structural dynamics of intact human IgG₁ molecules. The flexibility of different IgG subclasses is a function of the sequence and length of the Fab–Fc hinge region [57], and the human IgG₁ subclass shows the most interdomain flexibility, with Fab–Fc angles ranging from 60° to 160° [58]. We employed SAXS analysis to evaluate the flexibility of the corresponding FVIII–Fc junction, and found that a similar range of flexibility in solution was shown by the resulting ensemble model, a finding that was corroborated by negative-stain EM analysis.

We further assessed the dynamics of the FVIII–Fc junction by comparing the affinities for rFVIII/rFVIII-Fc of

Fig. 5. Binding of ESH8, GMA-8014 and GMA-8008 to recombinant factor VIII (rFVIII) and recombinant FVIII Fc (rFVIII-Fc). (A) The epitopes on FVIII of three different anti-C2 antibodies are highlighted in yellow (FVIII domains are colored as in Figure 2, with the C terminus in cyan). (B) Representative class averages of negatively stained B-domain-deleted rFVIII in complex with the Fab of each antibody show that these antibodies bind to FVIII in a position similar to that occupied by Fc in rFVIII-Fc (Fig. 4). See Fig. S9 for all class averages. The side length of the individual panels is 27.3 nm. (C) The affinities of each antibody for rFVIII and rFVIII-Fc were determined by surface plasmon resonance in triplicate, and indicate that the presence of Fc in rFVIII-Fc does not affect the binding of these antibodies to FVIII. RU, resonance units.

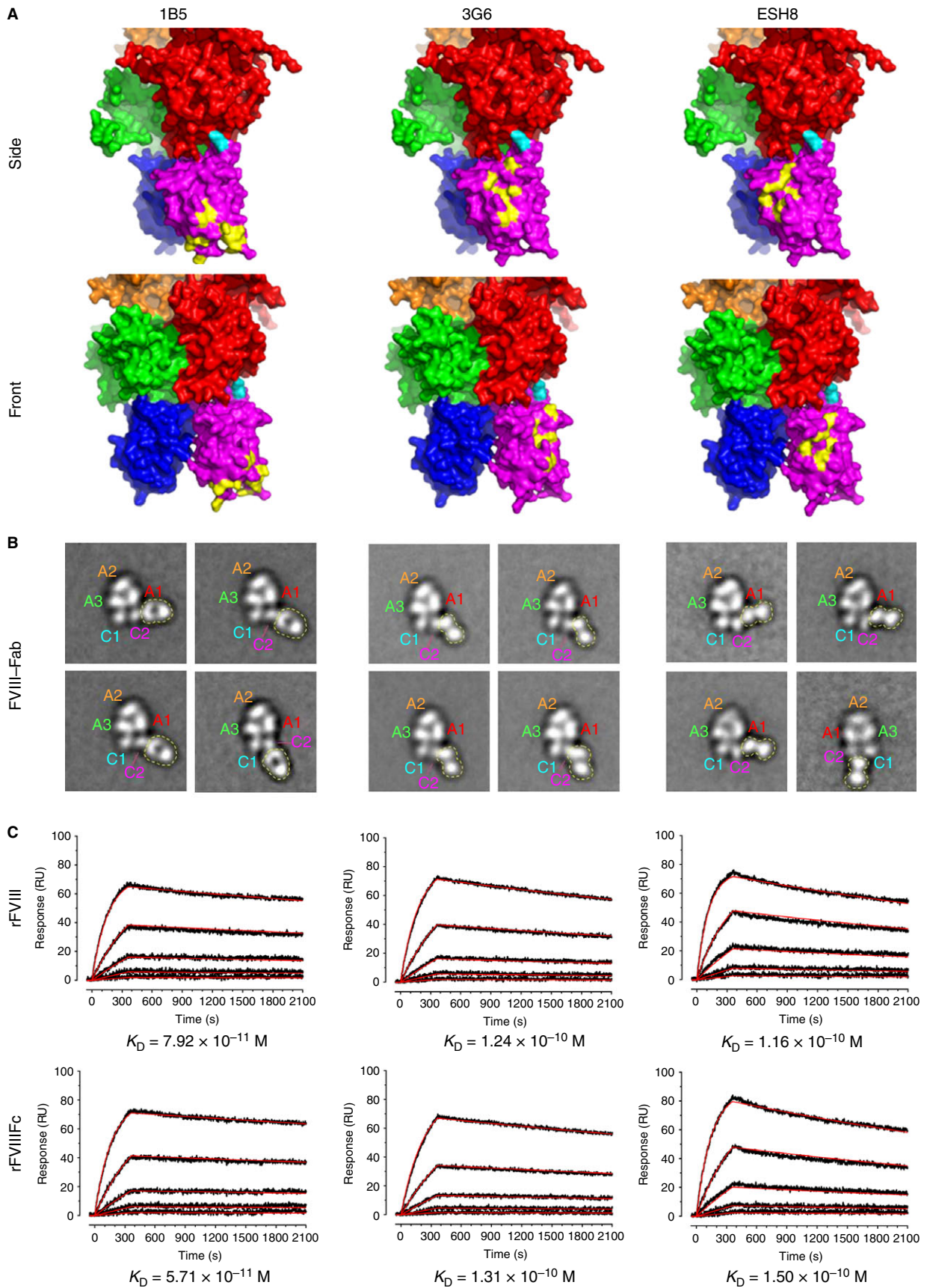


Table 2 Affinities of anti-C2 antibodies for recombinant factor VIII (rFVIII) and recombinant human B-domain-deleted FVIII Fc (rFVIII-Fc) (K_D)

	1B5	3G6	ESH8
rFVIII			
Run 1	7.92×10^{-11} M	1.24×10^{-10} M	1.16×10^{-10} M
Run 2	7.56×10^{-11} M	1.17×10^{-10} M	1.13×10^{-10} M
Run 3	6.61×10^{-11} M	1.23×10^{-10} M	0.98×10^{-10} M
Average	7.36×10^{-11} M	1.21×10^{-10} M	1.10×10^{-10} M
rFVIII-Fc			
Run 1	9.48×10^{-11} M	1.31×10^{-10} M	1.50×10^{-10} M
Run 2	5.71×10^{-11} M	1.37×10^{-10} M	1.43×10^{-10} M
Run 3	6.90×10^{-11} M	1.21×10^{-10} M	1.45×10^{-10} M
Average	7.36×10^{-11} M	1.30×10^{-10} M	1.46×10^{-10} M

three well-characterized anti-C2 antibodies, each with distinctly different epitopes, inhibitory activities, and potencies for inhibiting the association of FVIII with phospholipid surfaces and VWF. It is of particular note that antibody 1B5 potently inhibits both phospholipid and VWF binding by FVIII, consistent with the mapping of its epitope to the phospholipid-binding ‘feet’ of the C2 domain [52], whereas antibody 3G6 is a potent type II inhibitor (25 000 Bethesda units mg^{-1}) that impairs the activation of FVIII by either thrombin or FXa, but causes only slight inhibition of FVIII binding to either phospholipid or VWF [21]. Each antibody showed similar affinities for FVIII and rFVIII-Fc, demonstrating that, despite the proximity of their respective epitopes to the FVIII-Fc junction (29 Å for 1B5; 17 Å for 3G6; and 19 Å for ESH8) and the distinctly different mechanisms underlying their inhibition of FVIII procoagulant activity, the appended Fc domain of rFVIII-Fc did not sterically interfere with their binding to the FVIII C2 domain. These findings support the conclusion that the Fc domain of rFVIII-Fc dynamically samples a wide range of conformational space in relation to FVIII, as illustrated in Movie S1. This evidence of flexible tethering and the demonstration that the FVIII and Fc components of rFVIII-Fc are structurally indistinguishable from their isolated counterparts provide a structural rationale for the previously reported functional comparability of FVIII and its long-acting variant, rFVIII-Fc.

Acknowledgements

The authors thank A. Mezo, D. Light, J. Arndt, G. Pierce, and J. Tainer for their contributions. Use of the APS was supported by the US Department of Energy, Office of Science, Office of Basic Energy Sciences, under Contract No. DE-AC02-06CH11357. Use of the LRL-CAT beamline facilities at Sector 31 of the APS was provided by Eli Lilly & Company, which operates the facility. SIBYLS was supported by the US Department of Energy, Integrated Diffraction Analysis Technologies program and NIH MINOS R01GM105404. Coordinates and structure factors of the rFVIII-Fc

crystal structure have been deposited in the PDB with accession code 5K8D.

Addendum

J. D. Kulman and R. T. Peters conceived the study. N. C. Leksa, P.-L. Chiu, G. M. Bou-Assaf, C. Quan, Z. Liu, A. B. Goodman, M. G. Chambers, S. E. Tsutakawa, M. Hammel, and T. Walz performed and analyzed experiments. N. C. Leksa, J. D. Kulman, and T. Walz wrote the manuscript with contributions from all authors.

Disclosure of Conflict of Interests

N. C. Leksa, G. M. Bou-Assaf, C. Quan, Z. Liu, A. B. Goodman, R. T. Peters and J. D. Kulman were employees of Biogen at the time of this work. P.-L. Chiu, S. E. Tsutakawa, M. Hammel and T. Walz received funding support from Biogen. This work was funded by Biogen/Bioverativ.

Supporting Information

Additional Supporting Information may be found in the online version of this article:

Fig. S1. Pair distribution function of rFVIII and rFVIII-Fc. (A) The Guinier plots for the experimental SAXS profiles are shown. The magenta line represents the linear fit to the Guinier region with the limit $qRG < 1.6$ and indicates an aggregation-free state of the samples. (B) Experimental (black) and theoretical (red) $P(r)$ functions of rFVIII were calculated from the experimental and theoretical SAXS profiles shown in Fig. 3A. (C) Experimental $P(r)$ function (black) of rFVIII-Fc compared to the theoretical $P(r)$ functions calculated for the best fit model (red) and the ensemble model (green) shown in Fig. 3C.

Fig. S2. Image pair of a specimen area of negatively stained rFVIII-Fc recorded at tilt angles of 0° and 60° . The lines indicate the tilt axis. Scale bar indicates 100 nm.

Fig. S3. The class averages of negatively stained rFVIII-Fc that were obtained with the iterative stable alignment and classification (ISAC) algorithm. The 16,158 particles selected from the images of untilted specimens were subjected to 25 ISAC generations, yielding 475 class averages. The side length of the individual panels is 27.3 nm.

Fig. S4. The class averages of negatively stained rFVIII-Fc that were obtained with K-means classification. (A) The 16,158 particles selected from the images of untilted specimens were subjected to K-means classification into 100 classes. The averages are ordered from the most populated class at the top left to the least populated class at the bottom right. (B) The panels to the left show the seven averages that were chosen as references for supervised classification. The panels to the right show the resulting class averages. The numbers indicate the 3D

density maps that are shown in Fig. 4. The side length of the individual panels is 27.3 nm.

Fig. S5. Fourier shell correlation (FSC) curves for the six density maps obtained with negatively stained rFVIII Fc. According to the FSC = 0.5 cut-off criterion, the resolution of the density maps ranges from 2.5 to 3 nm.

Fig. S6. Placement of FVIII and Fc crystal structures into EM density maps. The crystal structures of FVIII (PDB code: 3CDZ) and Fc (PDB code: 1HZH) were placed into EM density maps 1 (A), 4 (B) and 6 (C). The scale bar is 5 nm.

Fig. S7. rFVIII Fc peptide coverage map for HDX-MS. The sequences of the FVIII-Fc monomer (A) and the separately expressed Fc monomer (B) are shown. Blue bars below the sequence indicate peptides from rFVIII Fc identified by MS. For FVIII and Fc, 94% and 87% of the expected peptides were recovered, respectively, and used to determine deuterium exchange.

Fig. S8. Silver-stained reducing SDS-PAGE gel of a dissolved rFVIII Fc crystal. The first lane contains purified rFVIII Fc prior to crystallization, and the second lane contains a dissolved crystal, confirming the presence of the Fc. All bands are present at the expected relative intensities.

Fig. S9. Negative-stain EM analysis of BDD rFVIII in complex with Fabs of anti-C2 antibodies. (A) Raw image of negatively stained complex of BDD rFVIII with Fabs of EHS8. Scale bar indicates 50 nm. (B-D) The averages that were obtained by K-means classification of negatively stained BDD rFVIII in complex with Fabs of EHS8 (B), Fabs of GMA-8014 (C), and Fabs of GMA-8008 (D). The side length of the individual panels is 25.6 nm.

Movie S1. Mobility of the Fc domain relative to the FVIII component in rFVIII Fc. Selected ISAC averages of rFVIII Fc were aligned to one another and ordered according to their correlation coefficients to visualize the flexibility of the appended Fc.

Table S1. Data collection and refinement statistics.

Table S2. Data collection and SAXS parameters.

References

- Peyvandi F, Jayandharan G, Chandy M, Srivastava A, Nakaya SM, Johnson MJ, Thompson AR, Goodeve A, Garagiola I, Lavoretano S, Menegatti M, Palla R, Spreafico M, Tagliabue L, Asselta R, Duga S, Mannucci PM. Genetic diagnosis of haemophilia and other inherited bleeding disorders. *Haemophilia* 2006; **12**(Suppl. 3): 82–9.
- Valentino LA, Mamonov V, Hellmann A, Quon DV, Chybicka A, Schroth P, Patrone L, Wong WY; Prophylaxis Study Group. A randomized comparison of on-demand and prophylaxis treatments in hemophilia A management. *J Thromb Haemost* 2012; **10**: 359–67.
- Nestorov I, Neelakantan S, Ludden TM, Li S, Jiang H, Rogge M. Population pharmacokinetics of recombinant factor VIII Fc fusion protein. *Clin Pharmacol Drug Dev* 2015; **4**: 163–74.
- Lillicrap D. Improvements in factor concentrates. *Curr Opin Hematol* 2010; **17**: 393–7.
- Harris JM, Chess RB. Effect of pegylation on pharmaceuticals. *Nat Rev Drug Discov* 2003; **2**: 214–21.
- Mei B, Pan C, Jiang H, Tjandra H, Strauss J, Chen Y, Liu T, Zhang X, Severs J, Newgren J, Chen J, Gu JM, Subramanyam B, Fournel MA, Pierce GF, Murphy JE. Rational design of a fully active, long-acting PEGylated factor VIII for hemophilia A treatment. *Blood* 2010; **116**: 270–9.
- Turecek PL, Bossard MJ, Graninger M, Gritsch H, Hollriegel W, Kaliwoda M, Matthiessen P, Mitterer A, Muchitsch EM, Purtscher M, Rottensteiner H, Schiviz A, Schrenk G, Siekmann J, Varadi K, Riley T, Ehrlich HJ, Schwarz HP, Scheiflinger F. BAX, 855, a PEGylated rFVIII product with prolonged half-life. Development, functional and structural characterisation. *Hamostaseologie* 2012; **32**(Suppl. 1): S29–38.
- Stennicke HR, Kjalke M, Karpf DM, Balling KW, Johansen PB, Elm T, Ovlisen K, Moller F, Holmberg HL, Gudme CN, Persson E, Hilden I, Pelzer H, Rahbek-Nielsen H, Jespersgaard C, Bogsnes A, Pedersen AA, Kristensen AK, Peschke B, Kappers W, *et al.* A novel B-domain O-glycoPEGylated FVIII (N8-GP) demonstrates full efficacy and prolonged effect in hemophilic mice models. *Blood* 2013; **121**: 2108–16.
- Konkle BA, Stasyshyn O, Chowdary P, Bevan DH, Mant T, Shima M, Engl W, Dyck-Jones J, Fuerlinger M, Patrone L, Ewenstein B, Abbuehl B. Pegylated, full-length, recombinant factor VIII for prophylactic and on-demand treatment of severe hemophilia A. *Blood* 2015; **126**: 1078–85.
- Dumont JA, Liu T, Low SC, Zhang X, Kamphaus G, Sakorafas P, Fraley C, Drager D, Reidy T, McCue J, Franck HW, Merricks EP, Nichols TC, Bitonti AJ, Pierce GF, Jiang H. Prolonged activity of a recombinant factor VIII-Fc fusion protein in hemophilia A mice and dogs. *Blood* 2012; **119**: 3024–30.
- Peters RT, Toby G, Lu Q, Liu T, Kulman JD, Low SC, Bitonti AJ, Pierce GF. Biochemical and functional characterization of a recombinant monomeric factor VIII-Fc fusion protein. *J Thromb Haemost* 2013; **11**: 132–41.
- Dumont JA, Loveday KS, Light DR, Pierce GF, Jiang H. Evaluation of the toxicology and pharmacokinetics of recombinant factor VIII Fc fusion protein in animals. *Thromb Res* 2015; **136**: 1266–72.
- Mahlangu J, Powell JS, Ragni MV, Chowdary P, Josephson NC, Pabinger I, Hanabusa H, Gupta N, Kulkarni R, Fogarty P, Perry D, Shapiro A, Pasi KJ, Apte S, Nestorov I, Jiang H, Li S, Neelakantan S, Cristiano LM, Goyal J, *et al.* Phase 3 study of recombinant factor VIII Fc fusion protein in severe hemophilia A. *Blood* 2014; **123**: 317–25.
- Shapiro AD, Ragni MV, Kulkarni R, Oldenberg J, Srivastava A, Quon DV, Pasi KJ, Hanabusa H, Pabinger I, Mahlangu J, Fogarty P, Lillicrap D, Kulke S, Potts J, Neelakantan S, Nestorov I, Li S, Dumont JA, Jiang H, Brennan A, *et al.* Recombinant factor VIII Fc fusion protein: extended-interval dosing maintains low bleeding rates and correlates with von Willebrand factor levels. *J Thromb Haemost* 2014; **12**: 1788–800.
- Nolan B, Mahlangu J, Perry D, Young G, Liesner R, Konkle B, Rangarajan S, Brown S, Hanabusa H, Pasi KJ, Pabinger I, Jackson S, Cristiano LM, Li X, Pierce GF, Allen G. Long-term safety and efficacy of recombinant factor VIII Fc fusion protein (rFVIII Fc) in subjects with haemophilia A. *Haemophilia* 2016; **22**: 72–80.
- Saenko EL, Scandella D. The acidic region of the factor VIII light chain and the C2 domain together form the high affinity binding site for von Willebrand factor. *J Biol Chem* 1997; **272**: 18007–14.
- Saenko EL, Shima M, Rajalakshmi KJ, Scandella D. A role for the C2 domain of factor VIII in binding to von Willebrand factor. *J Biol Chem* 1994; **269**: 11601–5.
- Shima M, Scandella D, Yoshioka A, Nakai H, Tanaka I, Kamisue S, Terada S, Fukui H. A factor VIII neutralizing monoclonal

- antibody and a human inhibitor alloantibody recognizing epitopes in the C2 domain inhibit factor VIII binding to von Willebrand factor and to phosphatidylserine. *Thromb Haemost* 1993; **69**: 240–6.
- 19 Chiu PL, Bou-Assaf GM, Chhabra ES, Chambers MG, Peters RT, Kulman JD, Walz T. Mapping the interaction between factor VIII and von Willebrand factor by electron microscopy and mass spectrometry. *Blood* 2015; **126**: 935–8.
 - 20 Yee A, Oleskie AN, Dosey AM, Kretz CA, Gildersleeve RD, Dutta S, Su M, Ginsburg D, Skiniotis G. Visualization of an N-terminal fragment of von Willebrand factor in complex with factor VIII. *Blood* 2015; **126**: 939–42.
 - 21 Meeks SL, Healey JF, Parker ET, Barrow RT, Lollar P. Antihuman factor VIII C2 domain antibodies in hemophilia A mice recognize a functionally complex continuous spectrum of epitopes dominated by inhibitors of factor VIII activation. *Blood* 2007; **110**: 4234–42.
 - 22 Pratt KP, Qian J, Ellaban E, Okita DK, Diethelm-Okita BM, Conti-Fine B, Scott DW. Immunodominant T-cell epitopes in the factor VIII C2 domain are located within an inhibitory antibody binding site. *Thromb Haemost* 2004; **92**: 522–8.
 - 23 McCue JT, Selvitelli K, Walker J. Application of a novel affinity adsorbent for the capture and purification of recombinant factor VIII compounds. *J Chromatogr A* 2009; **1216**: 7824–30.
 - 24 McCue J, Kshirsagar R, Selvitelli K, Lu Q, Zhang M, Mei B, Peters R, Pierce GF, Dumont J, Raso S, Reichert H. Manufacturing process used to produce long-acting recombinant factor VIII Fc fusion protein. *Biologicals* 2015; **43**: 213–19.
 - 25 Houde D, Berkowitz SA, Engen JR. The utility of hydrogen/deuterium exchange mass spectrometry in biopharmaceutical comparability studies. *J Pharm Sci* 2011; **100**: 2071–86.
 - 26 Otwinowski Z, Minor W. Processing of X-ray diffraction data collected in oscillation mode. In: Carter Jr CW, Sweet RM, eds. *Methods in Enzymology*. New York: Academic Press, 1997: 307–26.
 - 27 McCoy AJ, Grosse-Kunstleve RW, Adams PD, Winn MD, Storoni LC, Read RJ. Phaser crystallographic software. *J Appl Crystallogr* 2007; **40**: 658–74.
 - 28 Shen BW, Spiegel PC, Chang CH, Huh JW, Lee JS, Kim J, Kim YH, Stoddard BL. The tertiary structure and domain organization of coagulation factor VIII. *Blood* 2008; **111**: 1240–7.
 - 29 Emsley P, Lohkamp B, Scott WG, Cowtan K. Features and development of Coot. *Acta Crystallogr D Biol Crystallogr* 2010; **66**: 486–501.
 - 30 Winn MD, Ballard CC, Cowtan KD, Dodson EJ, Emsley P, Evans PR, Keegan RM, Krissinel EB, Leslie AG, McCoy A, McNicholas SJ, Murshudov GN, Pannu NS, Potterton EA, Powell HR, Read RJ, Vagin A, Wilson KS. Overview of the CCP4 suite and current developments. *Acta Crystallogr D Biol Crystallogr* 2011; **67**: 235–42.
 - 31 Murshudov GN, Skubak P, Lebedev AA, Pannu NS, Steiner RA, Nicholls RA, Winn MD, Long F, Vagin AA. REFMAC5 for the refinement of macromolecular crystal structures. *Acta Crystallogr D Biol Crystallogr* 2011; **67**: 355–67.
 - 32 Nicholls RA, Long F, Murshudov GN. Low-resolution refinement tools in REFMAC5. *Acta Crystallogr D Biol Crystallogr* 2012; **68**: 404–17.
 - 33 Winn MD, Isupov MN, Murshudov GN. Use of TLS parameters to model anisotropic displacements in macromolecular refinement. *Acta Crystallogr D Biol Crystallogr* 2001; **57**: 122–33.
 - 34 Schrodinger LLC. The PyMOL Molecular Graphics System, Version 1.8. 2015.
 - 35 Classen S, Hura GL, Holton JM, Rambo RP, Rodic I, McGuire PJ, Dyer K, Hammel M, Meigs G, Frankel KA, Tainer JA. Implementation and performance of SIBYLS: a dual endstation small-angle X-ray scattering and macromolecular crystallography beamline at the Advanced Light Source. *J Appl Crystallogr* 2013; **46**: 1–13.
 - 36 Hura GL, Menon AL, Hammel M, Rambo RP, Poole FL 2nd, Tsutakawa SE, Jenney FE Jr, Classen S, Frankel KA, Hopkins RC, Yang SJ, Scott JW, Dillard BD, Adams MW, Tainer JA. Robust, high-throughput solution structural analyses by small angle X-ray scattering (SAXS). *Nat Methods* 2009; **6**: 606–12.
 - 37 Guinier A, Fournet F. *Small Angle Scattering of X-Rays*. New York: John Wiley & Sons Inc., 1955.
 - 38 Schneidman-Duhovny D, Hammel M, Tainer JA, Sali A. Accurate SAXS profile computation and its assessment by contrast variation experiments. *Biophys J* 2013; **105**: 962–74.
 - 39 Pelikan M, Hura GL, Hammel M. Structure and flexibility within proteins as identified through small angle X-ray scattering. *Gen Physiol Biophys* 2009; **28**: 174–89.
 - 40 Ohi M, Li Y, Cheng Y, Walz T. Negative staining and image classification – powerful tools in modern electron microscopy. *Biol Proced Online* 2004; **6**: 23–34.
 - 41 Shaikh TR, Gao H, Baxter WT, Asturias FJ, Boisset N, Leith A, Frank J. SPIDER image processing for single-particle reconstruction of biological macromolecules from electron micrographs. *Nat Protoc* 2008; **3**: 1941–74.
 - 42 Yang Z, Fang J, Chittuluru J, Asturias FJ, Penczek PA. Iterative stable alignment and clustering of 2D transmission electron microscope images. *Structure* 2012; **20**: 237–47.
 - 43 Hohn M, Tang G, Goodyear G, Baldwin PR, Huang Z, Penczek PA, Yang C, Glaeser RM, Adams PD, Ludtke SJ. SPARX, a new environment for Cryo-EM image processing. *J Struct Biol* 2007; **157**: 47–55.
 - 44 Radermacher M, Wagenknecht T, Verschoor A, Frank J. Three-dimensional reconstruction from a single-exposure, random conical tilt series applied to the 50S ribosomal subunit of *Escherichia coli*. *J Microsc* 1987; **146**: 113–36.
 - 45 Penczek PA, Grassucci RA, Frank J. The ribosome at improved resolution: new techniques for merging and orientation refinement in 3D cryo-electron microscopy of biological particles. *Ultramicroscopy* 1994; **53**: 251–70.
 - 46 Botchker B, Wynne SA, Crowther RA. Determination of the fold of the core protein of hepatitis B virus by electron cryomicroscopy. *Nature* 1997; **386**: 88–91.
 - 47 Pettersen EF, Goddard TD, Huang CC, Couch GS, Greenblatt DM, Meng EC, Ferrin TE. UCSF Chimera – a visualization system for exploratory research and analysis. *J Comput Chem* 2004; **25**: 1605–12.
 - 48 Ludtke SJ, Baldwin PR, Chiu W. EMAN: semiautomated software for high-resolution single-particle reconstructions. *J Struct Biol* 1999; **128**: 82–97.
 - 49 Bravman T, Bronner V, Lavie K, Notcovich A, Papalia GA, Myska DG. Exploring ‘one-shot’ kinetics and small molecule analysis using the ProteOn XPR36 array biosensor. *Anal Biochem* 2006; **358**: 281–8.
 - 50 Saphire EO, Parren PW, Pantophlet R, Zwick MB, Morris GM, Rudd PM, Dwek RA, Stanfield RL, Burton DR, Wilson IA. Crystal structure of a neutralizing human IGG against HIV-1: a template for vaccine design. *Science* 2001; **293**: 1155–9.
 - 51 Hammel M. Validation of macromolecular flexibility in solution by small-angle X-ray scattering (SAXS). *Eur Biophys J* 2012; **41**: 789–99.
 - 52 Nguyen PC, Lewis KB, Ettinger RA, Schuman JT, Lin JC, Healey JF, Meeks SL, Lollar P, Pratt KP. High-resolution mapping of epitopes on the C2 domain of factor VIII by analysis of point mutants using surface plasmon resonance. *Blood* 2014; **123**: 2732–9.
 - 53 Ragni MV. New and emerging agents for the treatment of hemophilia: focus on extended half-life recombinant clotting proteins. *Drugs* 2015; **75**: 1587–600.

- 54 Krishnamoorthy S, Liu T, Drager D, Patarroyo-White S, Chhabra ES, Peters R, Josephson N, Lillicrap D, Blumberg RS, Pierce GF, Jiang H. Recombinant factor VIII Fc (rFVIII_{FC}) fusion protein reduces immunogenicity and induces tolerance in hemophilia A mice. *Cell Immunol* 2016; **301**: 30–9.
- 55 Young G, Mahlangu J, Kulkarni R, Nolan B, Liesner R, Pasi J, Barnes C, Neelakantan S, Gambino G, Cristiano LM, Pierce GF, Allen G. Recombinant factor VIII Fc fusion protein for the prevention and treatment of bleeding in children with severe hemophilia A. *J Thromb Haemost* 2015; **13**: 967–77.
- 56 Ngo JC, Huang M, Roth DA, Furie BC, Furie B. Crystal structure of human factor VIII: implications for the formation of the factor IXa–factor VIIIa complex. *Structure* 2008; **16**: 597–606.
- 57 Roux KH, Strelets L, Michaelsen TE. Flexibility of human IgG subclasses. *J Immunol* 1997; **159**: 3372–82.
- 58 Zhang X, Zhang L, Tong H, Peng B, Rames MJ, Zhang S, Ren G. 3D structural fluctuation of IgG1 antibody revealed by individual particle electron tomography. *Sci Rep* 2015; **5**: 9803.